

Supplementary Information

Molecularly-Anchored Single PbS Quantum Dots as Resonant Tunnelling Transistors

Retno Dwi Wulandari,^{a,b,c} Dongbao Yin,^a Ricky Dwi Septianto,^{b,c} Seiichiro Izawa,^a Yoshihiro Iwasa,^b Satria Zulkarnaen Bisri,^{b,c*} and Yutaka Majima^{a*}

^aMaterials and Structures Laboratory, Institute of Integrated Research, Institute of Science Tokyo, 4259 Nagatsuta-cho, Midori-ku, Yokohama, Kanagawa 226-8503, Japan

^bRIKEN Center for Emergent Matter Science (CEMS), 2-1 Hirosawa, Wako, Saitama 351-0198, Japan

^cDepartment of Applied Physics and Chemical Engineering, Tokyo University of Agriculture and Technology, 2-26 Nakacho, Koganei, Tokyo 184-8588, Japan

Corresponding Author

Yutaka Majima, e-mail: majima@msl.titech.ac.jp

Satria Zulkarnaen Bisri, e-mail: satria-bisri@go.tuat.ac.jp

Supplementary Note 1: PbS colloidal quantum dots

A. Morphology characterisation and absorption spectra of lead sulphide (PbS) colloidal QDs

In this work, we used 8.1 nm PbS QDs, the size of which is determined by measuring the diameter from the TEM image, as shown in Figure S1. The size distribution was collected from more than 200 particles in the sample. UV-VIS-NIR absorption spectroscopy evaluated the sample's optical properties, and the absorbance spectrum was recorded in Figure S2. The PbS QDs exhibit well-defined excitonic peaks and valleys with a high peak-to-valley ratio. The associated excitonic peaks are at 1865 nm, indicating 8.1 ± 0.4 nm of QD size.

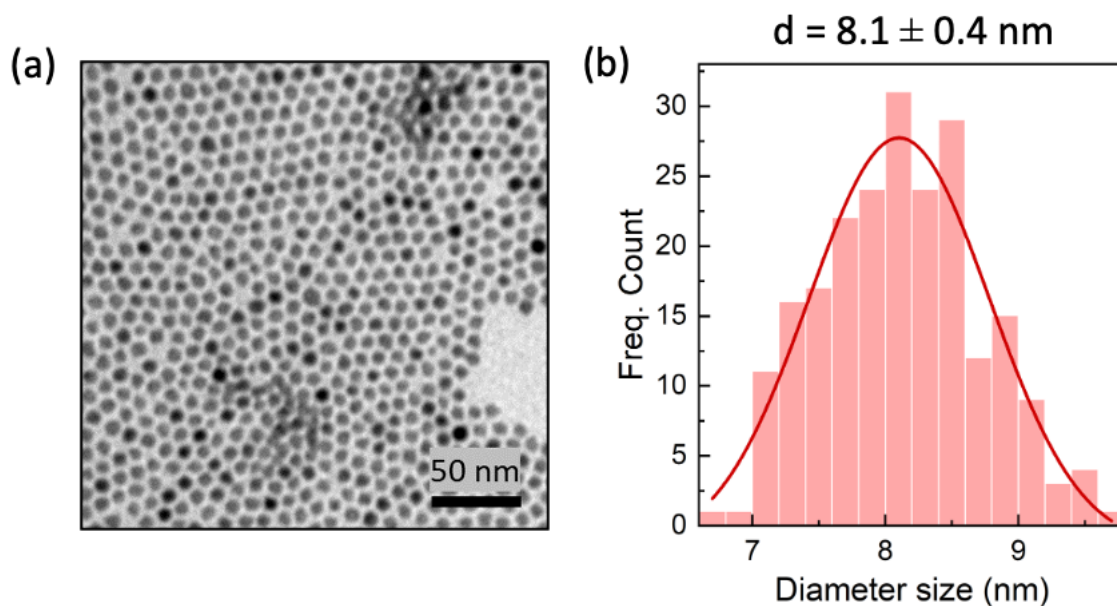


Figure S1. (a) Transmission electron microscopy (TEM) of PbS QDs and (b) the corresponding histogram size distribution of PbS QDs showing an average of 8.1 ± 0.4 nm of diameter size.

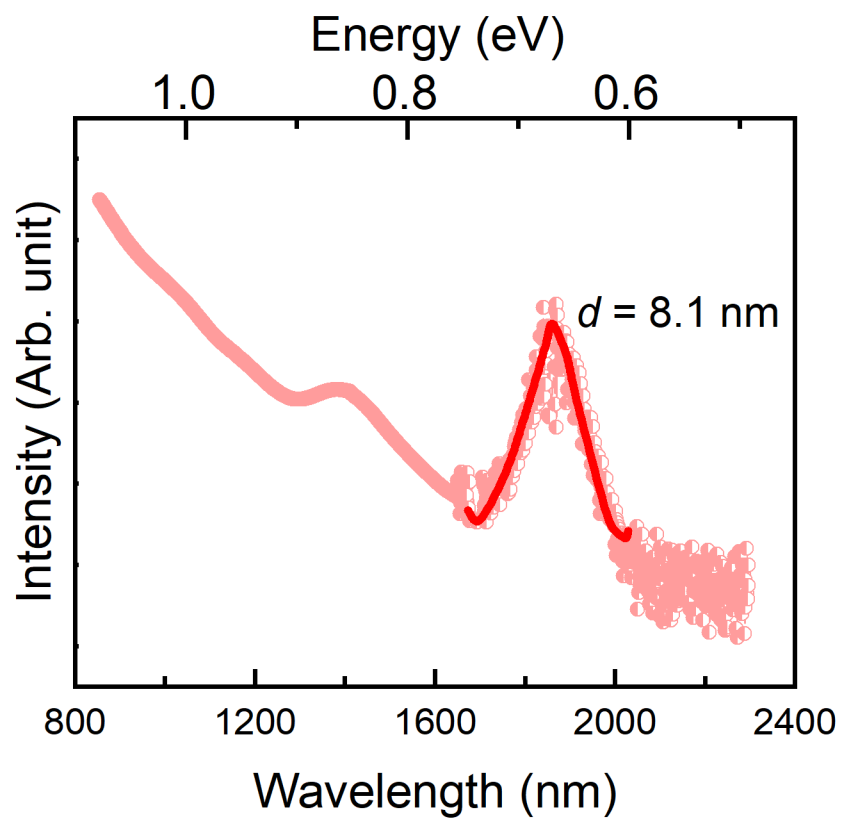


Figure S2. The absorption spectra of PbS QDs. Well-defined excitonic peaks and valleys were observed in 1860 and 1680 nm, respectively.

Supplementary Note 2: Electroless Au-plated (ELGP) heteroepitaxial spherical Au/Pt nanogap electrodes

Nanogap electrodes are a platform for nanodevices that enable the utilisation of the electrical characteristics of many nanostructured materials by interconnecting these structures with two terminals, thus integrating nanometre-size molecules into macroscopic electronic circuits.¹⁻³ By combining bottom-up and top-down processes, we have established the fabricate processes for electroless Au-plated (ELGP) heteroepitaxial spherical (HS) Au/Pt nanogap electrodes with robust and precise structures at scales of a few nanometers. We used the ELGP method and an electron-beam lithography (EBL) process to fabricate robust HS-Au/Pt nanogap electrodes.

A. Procedure of electroless gold plating method (ELGP)^{2,3}

The ELGP process is explained by the following chemical reactions (1)-(4). Triiodide (I_3^-) is the critical component of the diluted iodine tincture that forms the base for the plating solution, which can be obtained by mixing potassium iodide (KI) and iodine (I_2), as shown in the chemical reaction (1) below.



I_3^- ions dissolve the pieces of Au leaves that are immersed in the solution by oxidising the metal from its solid state to form $[AuI_2]^-$ ions and subsequently $[AuI_4]^-$ ions, which are shown in chemical reactions (2) and (3), respectively.



During this plating process at room temperature, Au is generated from the $[AuI_4]^-$ through the formation of $[AuI_2]^-$. Owing to the surface-catalysed reaction at the Pt electrodes, Au ions of $[AuI_2]^-$ are electroless plated by introducing the reducing agent, *L*(+)-ascorbic acid ($C_6H_8O_6$). Because the solution is saturated with *L*(+)-ascorbic acid, the triiodide by-product I_3^- is then transformed into I^- with dehydroascorbic acid as the product, which prevents etching of the Pt electrodes and can reversibly oxidise iodide into triiodide depending on the availability of $2H^+$ as following reaction.^{5,6}



The electroless plating process continues as long as both the plating $[AuI_2]^-$ ions and the *L*(+)-ascorbic acid are available at the surface of the Pt electrodes. The growth of the plating layer in the nanogap between the Pt electrodes is self-terminated due to the mass transport of the

plating $[\text{AuI}_2]^-$ ions into the nanogap region is restricted. The probability that the ions and reducing agent access the nanogap is decreased as the gap narrows; however, the plating layer grows continuously in other areas. Therefore, as the gap separation decreases, the electroless plating rate between the electrodes also decreases, and self-termination of ELGP between the nanogap occurs due to the obstruction of mass transport of $[\text{AuI}_2]^-$ ions between the nanogap. Figures 3(a) and (b) show that the ELGP process can push our nanogap narrower from 14.88 nm to 9.36 nm, respectively.

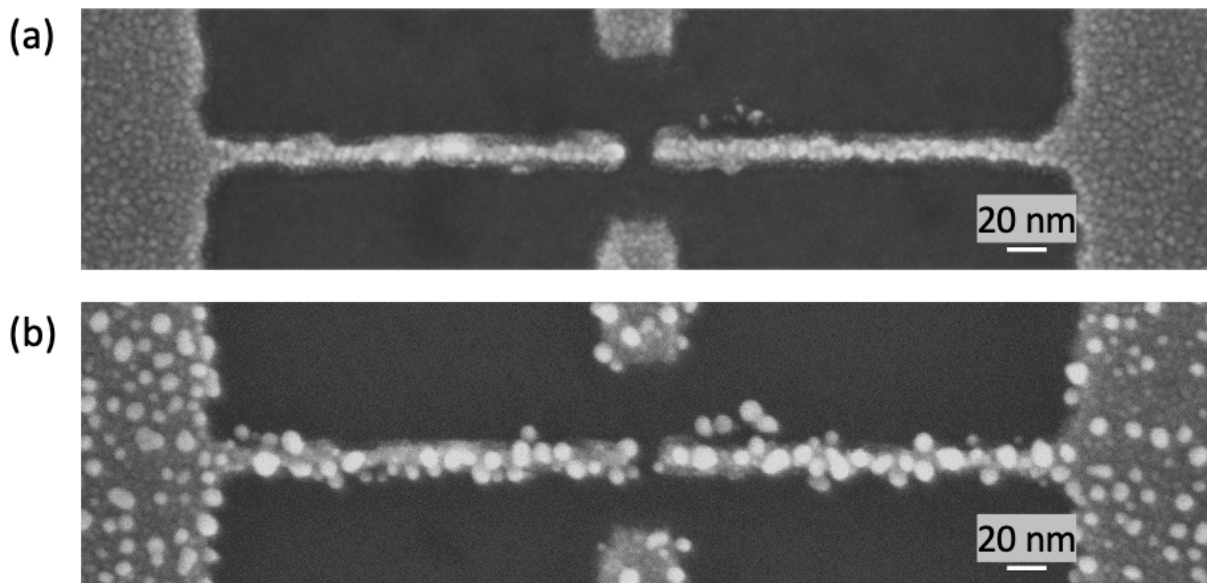


Figure S3. (top view) SEM image of (a) ultrafine-linewidth initial Pt nanogap electrodes fabricated by electron beam lithography (EBL) on SiO_2/Si substrate⁴ before the ELGP process, and (b) ELGP heteroepitaxial spherical Au/Pt nanogap electrodes.

Supplementary Note 3: Yield of working devices and NDR devices

In this research, we measured 8 chips of nanogap electrodes, each containing 44 devices, for a total of 352 devices. The heteroepitaxial spherical (HS)-Au/Pt nanogap electrodes were fabricated using a combination of electroless gold plating (ELGP) and electron beam lithography (EBL), achieving a high fabrication yield of 90% without any short circuits.

Among the fabrication devices, the yield of working devices, defined as those showing drain current flows of more than 10 pA under an application of drain voltage up to 2 V, was 43.7%. This yield excludes devices exhibiting short circuits or noise signals, reflecting the stability of the nanogap electrodes and the reliability of the fabrication process.

However, achieving NDR properties requires precise molecular anchoring of the PbS QD to the source or drain electrodes via short, bidentate thiol ligands to ensure robust Fermi-level pinning. As such, the yield of NDR devices was relatively lower than the working device yield, approximately 1.3%.

Additionally, the fabrication process described in this study demonstrates significant potential for scalability. The ability to produce 44 devices per chip, with a total of 352 devices fabricated across 8 chips, highlights the practicality of parallel device production. The high fabrication yield of 90% further supports its scalability. Two key factors enable this scalability:

1. Scalable QD capture: precise control of QD placement and ligand exchange ensures consistent device behaviour.
2. Robust nanogap electrodes: the reliability of ELGP-fabricated electrodes ensures uniformity and reproducibility across multiple devices.

While the yield of NDR devices (1.3%) remains low compared to working devices (43.7%), this challenge reflects the precision required for molecular anchoring and Fermi-level pinning. With further optimisation of QD deposition and ligand coupling process, this method provides a strong foundation for advancing scalable production of PbS QD RTT devices with NDR properties.

Supplementary Note 4: Negative differential resistance (NDR) in dI_D/dV_D - V_D characteristics

We observed hysteresis in the I_D - V_D characteristic, which is typically attributed to charge trapping or de-trapping phenomena at the interfaces within the device. Trapped charges can affect the local electric field, leading to a shift in the energy levels of the QD and affecting the conductance as the voltage is swept forward and backward. Additionally, the hysteresis might be influenced by slow relaxation processes within the QD or in the surrounding dielectric material, leading to a time-dependent response of the system to the applied voltage. This indicates that the electronic states within the device are not returning to their original configuration immediately after the voltage sweep, which is a common phenomenon in nanoscale electronic devices.

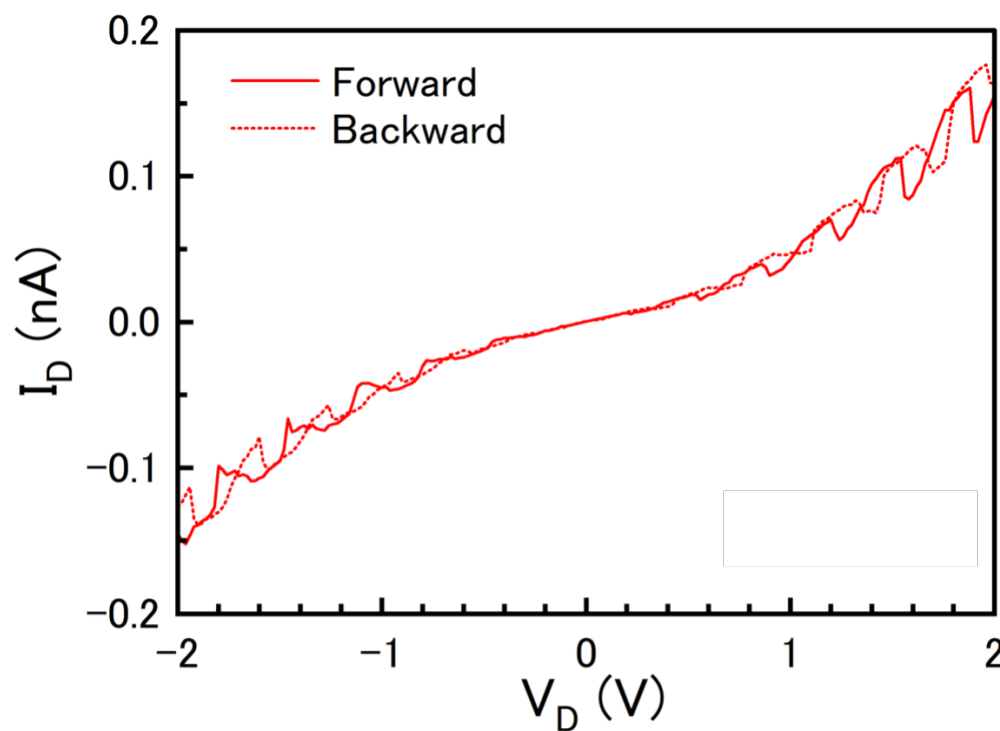


Figure S4. I_D - V_D characteristic of 1,4-butane-dithiol (BuDT)-anchored PbS QD RTT at $V_G = -2.19$ V showing the hysteresis between the forward and backward sweep bias directions.

From the differential conductance plot shown in Figure S5, the first conduction band peak is observed at a bias of approximately +0.3 V in the positive V_D regime, while the valence band peak is located at approximately -0.3 V in the negative V_D regime. This separation of around 0.6

V corresponds to the energy gap between the highest state of the valence band and the lowest state of the conduction band of the PbS QDs at low temperatures (9 K). The measured gap separation aligns closely with the optical band gap of 0.66 eV reported for PbS QDs at room temperature.

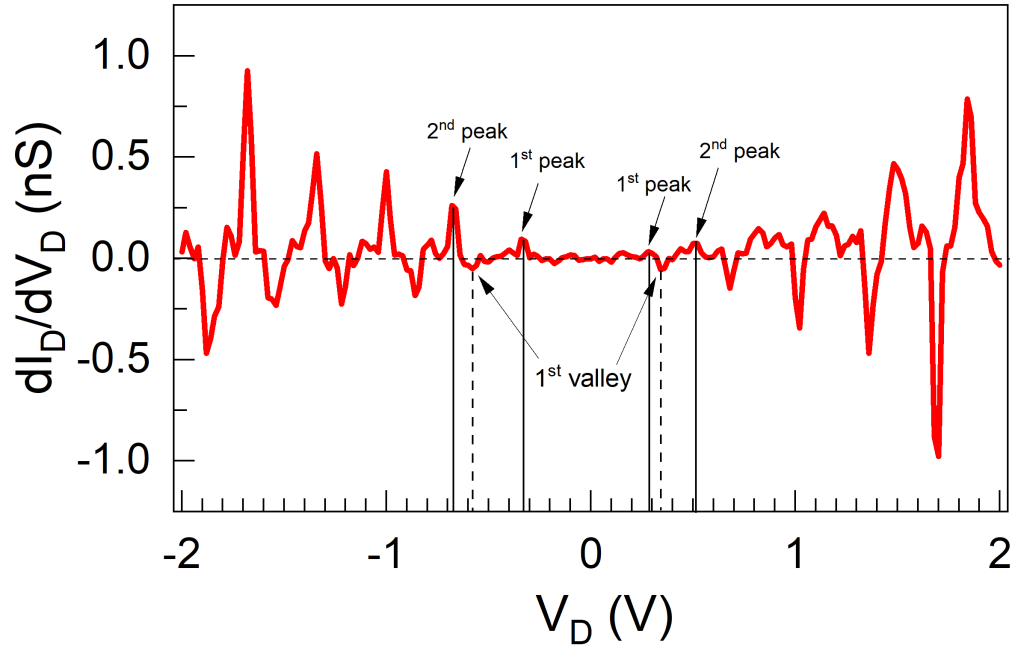


Figure S5. Differential conductance (dI_D/dV_D - V_D) characteristics of 1,4-butane-dithiol-anchored PbS QD RTT at $V_G = -2.19$ V. The peak-to-peak conductance spacing of NDRs and the gap separation between the first peak of positive and negative V_D regimes are shown.

Additionally, the peak-to-peak voltages of the NDR features range from 0.25 to 0.36 V, as determined by plotting the differential conductance as a function of V_D . These voltages correspond to the energy level spacing in the 1S state of our PbS QD.

The energy level spacing in QDs is governed by the quantum confinement effect and can be estimated using the relation:

$$\Delta E \approx \frac{\pi^2 \hbar^2}{2m^* \left(\frac{D}{2}\right)^2}$$

where \hbar is the reduced Plack's constant (1.054×10^{-34} Js), m^* is the effective electron mass, and D is the diameter of the quantum dot. For our PbS QDs ($D = 8.1$ nm, $m^* = 0.085m_0$),^{7,8} the calculated energy level spacing is approximately 275 meV.

This calculated value aligns with the observed peak-to-peak voltages and confirms that the NDR features arise from the energy level spacing in the 1S of our PbS QDs. The relatively large spacing is attributed to the small effective mass of PbS and the strong quantum confinement effect in the 8.1 nm diameter QDs.

The peak-valley ratio (PVR) of NDR is a key parameter in evaluating the performance of QD-RTTs. It is intrinsically related to the spacing between adjacent discrete energy levels in the QD. A higher PVR corresponds to a larger energy spacing between levels, while a lower PVR reflects a smaller spacing.

In this study, we analysed five distinct NDR peaks, with calculated PVR values of approximately 1.45, 1.32, 2.35, 1.27, and 1.32, as shown in **Figure S6**. The relatively uniform PVR values indicate that the energy level spacing within the 1S state of the PbS QD is nearly constant. This is consistent with the expected behaviour of quantum confinement in PbS QDs, which have four-fold degeneracy.

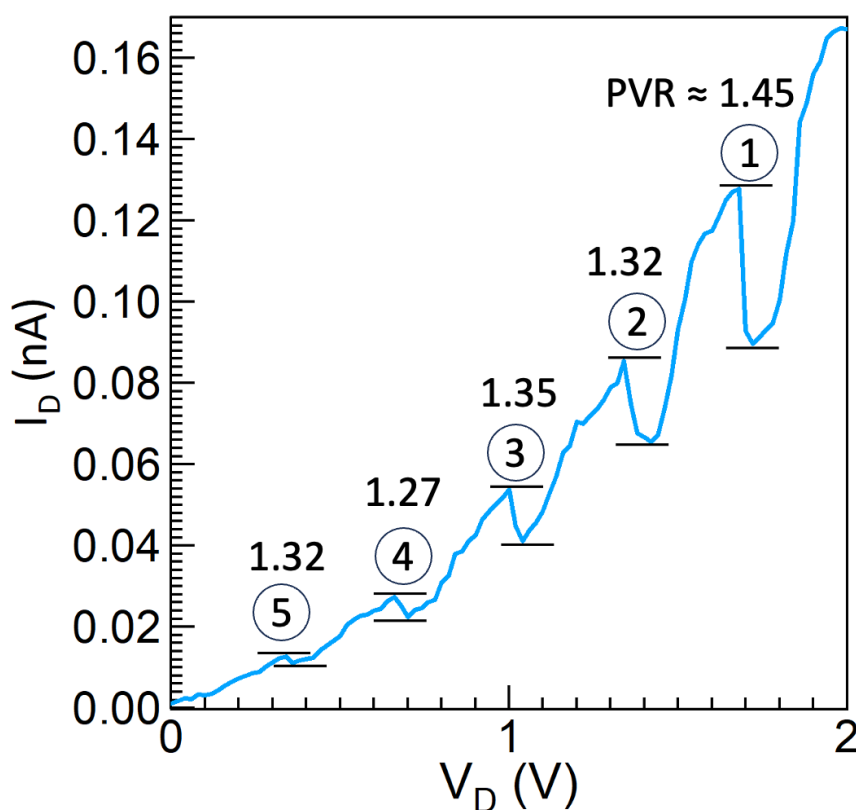


Figure S6. Enlarged I_D - V_D characteristics for the BuDT anchored PbS QD-RTT device at $V_G = -2.19$ V, highlighting five distinct NDR peaks and their corresponding PVR values. The relatively consistent PVR values across the peaks confirm the uniform energy level spacing in the 1S state of the PbS QD.

The following figures show the reproducibility of the multiple NDRs using a 1,4-butane-dithiol ligand anchored to the PbS QD RTT in another device. The multiple NDR properties are visible in both negative and positive V_D regimes.

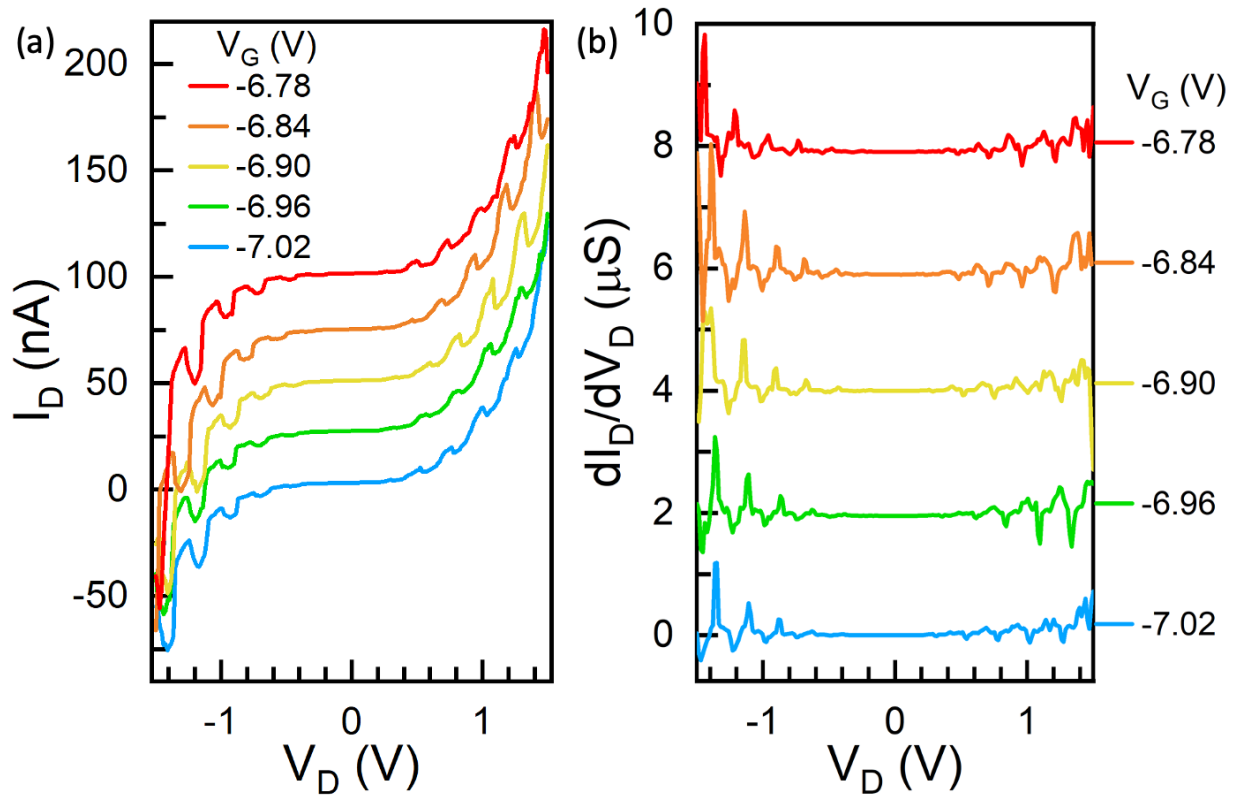


Figure S7. [Device 2] (a) The measured current-voltage (I_D - V_D) characteristics of 1,4-butane-dithiol-anchored PbS QD RTT at $T = 9$ K, taken at every 60-mV step of the back-gate voltage, V_G , showing multiple negative differential resistance (NDR) peaks in both negative and positive drain voltage (V_D) regime. The curves are offset by 25 nA for clarity. Only the bottom curve at $V_G = -7.02$ V corresponds to the scale. (b) The V_G dependence of differential conductance dI_D/dV_D was numerically calculated based on the experimental I_D - V_D characteristics, showing electronic states of PbS QD. The curves are offset by 2 μ S for clarity. Only the bottom curve at $V_G = -7.02$ V corresponds to the scale.

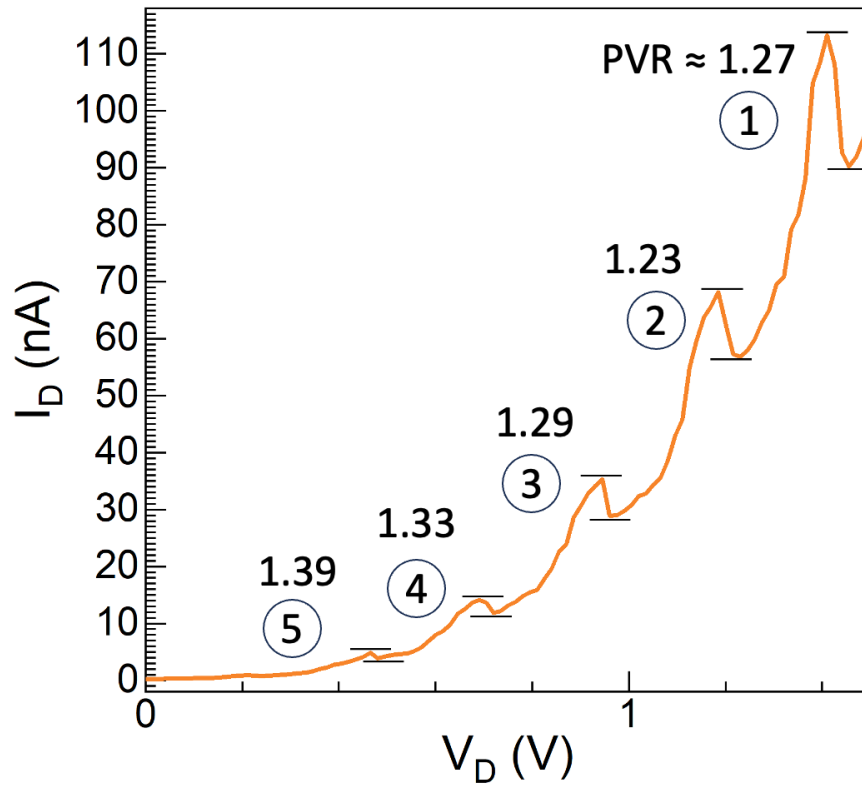


Figure S8. [Device 2] The estimated peak-to-valley current ratio (PVR) values of 1,4-butanedithiol-anchored PbS QDs RTT at $T = 9$ K for another same-structure device are approximately 1.27, 1.23, 1.29, 1.33, and 1.39.

We also use another shorter bidentate ligand, 1,2-ethanedithiol, to confirm that the bidentate ligand groups can strongly bond with Au. This gives us Fermi-level pinning, promoting NDR properties.

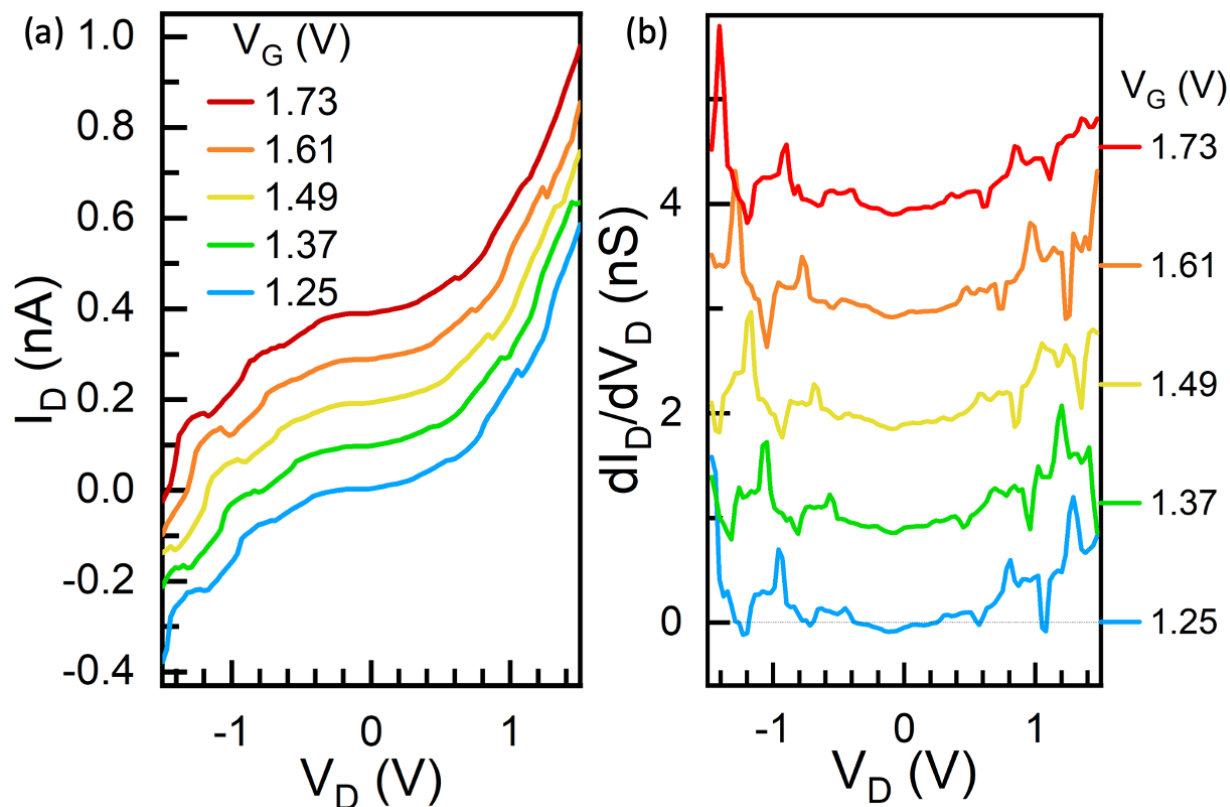


Figure S9. (a) The measured current-voltage (I_D - V_D) characteristics of 1,2-ethanedithiol-anchored PbS QD RTT at $T = 9$ K, taken at every 120-mV step of the back-gate voltage, V_G , showing multiple negative differential resistance (NDR) peaks in both negative and positive drain voltage (V_D) regime. (b) The V_G dependence of differential conductance dI_D/dV_D was numerically calculated based on the experimental I_D - V_D characteristics, showing electronic states of PbS QD. The curves are offset by 1 nS for clarity. Only the bottom curve at $V_G = 1.25$ V corresponds to the actual scale.

Supplementary Note 5: Coulomb oscillation in I_D - V_G characterisation

Oleic acid-capped PbS QD SETs

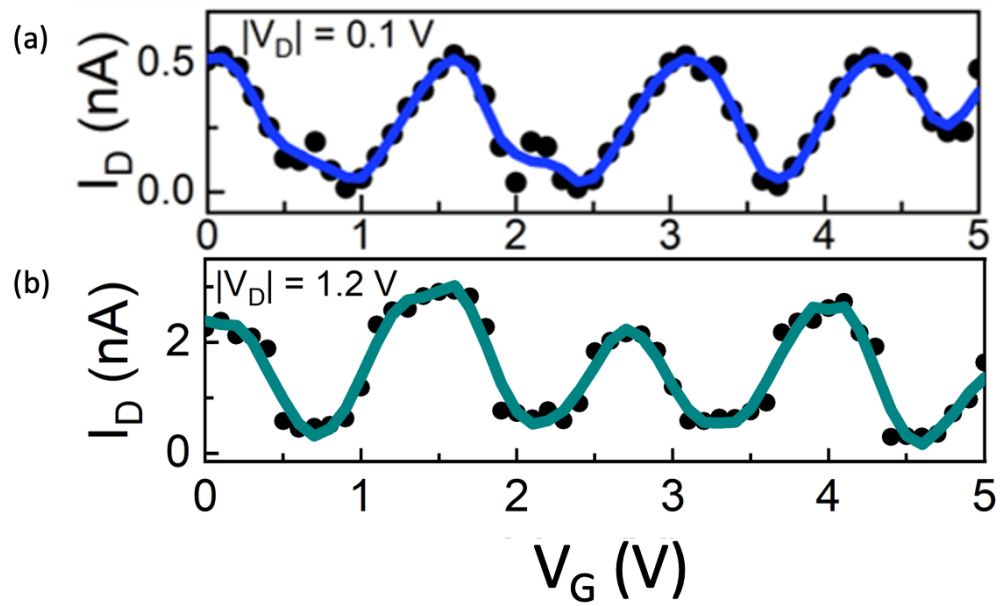


Figure S10. The measured drain current – back gate voltage characteristics of oleic acid-capped PbS QDs SETs for devices 1 and 2 at 9 K for all devices show clear Coulomb oscillations.

References

1. T. Li, W. Hu, and D. Zhu, *Adv. Mater.*, 2010, **22**, 286–300.
2. Y. Yasutake, K. Kono, M. Kanehara, T. Teranishi, M. R. Buitelaar, C. G. Smith, and Y. Majima, *Appl. Phys. Lett.*, 2007, **91**, 203107.
3. Y. Y. Choi, T. Teranishi, and Y. Majima, *Appl. Phys. Express*, 2019, **12**, 025002.
4. Y. Y. Choi, A. Kwon, and Y. Majima, *Appl. Phys. Express*, 2019, **12**, 125003.
5. M. Kataoka, S. Tahara, and K. Ohzeki, *Fresenius Z. Anal. Chem.*, 1985, **321**, 146–149.
6. M. Tarek, M. Zaki, and A. G. Abdel-Rehiem, *Mikrochim. Acta.*, 1986, **3**, 329–335.
7. I. Kang and F. W. Wise, *J. Opt. Soc. Am. B*, 1997, **14**, 1632-1646.
8. K. K. Nanda, F. E. Kruis, H. Fissan, and S. N. Bahera, *J. Appl. Phys.*, 2004, **95**, 5035-5041.